

Sub-gap spectroscopy of thermally excited quasiparticles in a Nb contacted carbon nanotube quantum dot

M. Gaass,¹ S. Pfaller,^{2,*} T. Geiger,¹ A. Donarini,² M. Grifoni,² A. K. Hüttel,¹ and Ch. Strunk^{1,†}

¹*Institute for Exp. and Applied Physics, University of Regensburg, 93040 Regensburg, Germany*

²*Institute for Theoretical Physics, University of Regensburg, 93040 Regensburg, Germany*

(Dated: June 7, 2021)

We present electronic transport measurements of a single wall carbon nanotube quantum dot coupled to Nb superconducting contacts. For temperatures comparable to the superconducting gap peculiar transport features are observed inside the Coulomb blockade and superconducting energy gap regions. The observed temperature dependence can be explained in terms of sequential tunneling processes involving thermally excited quasiparticles. In particular, these new channels give rise to two unusual conductance peaks at zero bias in the vicinity of the charge degeneracy point and allow to determine the degeneracy of the ground states involved in transport. The measurements are in good agreement with model calculations.

PACS numbers: 73.23.Hk, 73.63.Kv, 74.45.+c

Introduction– Carbon nanotubes (CNTs) are highly versatile quantum systems, whose properties can be investigated by attaching them to a wide variety of different contact materials.^{1–3} By using superconducting metals as electrodes, a significant increase of spectroscopic resolution due to the sharp peaks at the gap edges in the BCS density of states can be achieved.⁴ Depending on the coupling strength between the carbon nanotube and its leads, the nanotube can act as a Josephson weak link, and proximity-induced supercurrent can flow through the quantum dot.^{3,5–7} The supercurrent is carried by Andreev bound states, whose presence is revealed by peculiar subgap features.^{8–12} By fabricating the contacts from sputtered Nb, they can remain superconducting up to a critical temperature $T_c = 8.5$ K and a correspondingly large critical magnetic field B_c .

In this work we report on sub-gap features observed in a CNT quantum dot weakly coupled to superconducting leads. Strikingly, such features are not visible at the lowest temperatures achieved in the experiment but only when the temperature becomes comparable to the superconducting gap. This suggests that, as explained below, the observed sub-gap features are not due to Andreev reflections but rather to thermal excitation of quasiparticles across the gap, as predicted recently by some of us.¹³ We perform a systematic analysis of the temperature dependence of the observed features. A good agreement between experimental data and theoretical predictions in the linear as well as in the nonlinear regime is obtained.

Experimental details– The measurements presented here were performed on a single wall carbon nanotube grown by chemical vapour deposition (CVD).¹⁴ As substrate highly p-doped Si capped with 300 nm SiO_x is used. The electrodes to the nanotube are composed of 3 nm Pd as contact layer and 45 nm sputtered Nb with a contact spacing of the order of 300 nm. The room temperature resistance of our device is in the range of 100 k Ω .

For performing two- and four-point measurements, each superconducting electrode is connected to two AuPd leads as resistive on-chip elements that are, among other

filter stages, supposed to damp oscillations at the plasma frequency of the Josephson junction.^{7,15} A scanning elec-

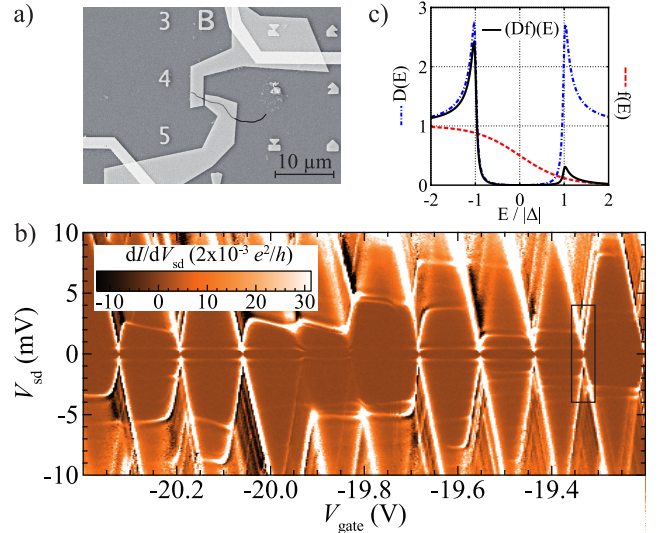


FIG. 1. (Color online) (a) Scanning electron micrograph of the measured device displaying the resistive AuPd leads (bright) and the Nb electrodes (faint). The location of the nanotube is indicated by the black curve. (b) Differential conductance $dI(V_{sd}, V_{gate})/dV_{sd}$ as a function of source-drain voltage V_{sd} and gate voltage V_{gate} at $T = 25$ mK. Dark areas correspond to negative differential conductance. The black rectangle outlines the parameter region of Fig. 2. (c) Scheme explaining the thermal excitation of quasiparticles across the superconducting gap, see text.

tron micrograph of the sample is shown in Fig. 1(a). The device was measured in a dilution refrigerator with a base temperature of 25 mK.

Transport spectroscopy– Fig. 1(b) shows an overview plot of the differential conductance dI/dV_{sd} as a function of source-drain voltage V_{sd} and gate voltage V_{gate} at $T = 25$ mK. This temperature is much smaller than the critical temperature T_c expected for our Nb con-

tacts. The measurement of Fig. 1(b) serves as a reference for the high temperature experiments and theoretical predictions discussed below. Besides regular Coulomb diamonds, a rich substructure of both elastic and inelastic cotunneling lines is observed,^{4,16,17} reflecting the high spectroscopic resolution brought about by the sharp peaks in the BCS density of states (cf. Fig. 1(c)).

The superconducting energy gap estimated from the sequential tunneling features at $V_{sd} = \pm 2\Delta/e$ (see details below) is $\Delta \sim 320 \mu\text{eV}$, compared to an expected value of $\Delta = 1.5 \text{ meV}$ for bulk Nb.¹⁸ This reduction of the gap has been reported before in similar Nb-based devices.^{4,12} Its origin so far remains an open question, though contamination of the lower Nb interface, formation of niobium oxide¹⁹, or the thin Pd contact layer may play a role.⁴ Estimated from $\Delta = 320 \mu\text{eV}$, the resulting effective critical temperature would be $T_c \sim 2.1 \text{ K}$. However, features in the data attributable to superconductivity remain present up to temperatures of about 3 K to 5 K, and measurements of a co-deposited Nb strip of comparable dimensions on the same chip yielded a critical temperature of $T_c = 8.5 \text{ K}$.

From additional stability diagrams similar to Fig. 1(b) but taken at higher temperatures and finite magnetic field to suppress superconductivity (not shown), we estimate a charging energy $U \sim 15 \text{ meV}$. From the fitting between experiments and theory discussed below (cf. in particular Eq. (4)), a coupling strength between quantum dot and leads of $\Gamma \sim 0.093 \text{ meV}$ is extracted. This places our measurement into the parameter range $\Gamma < \Delta \ll U$ where Coulomb repulsion dominates transport, superconductivity enhances the spectroscopic resolution,²⁰ and Andreev reflections are expected to be strongly suppressed.²¹ No obvious traces of Kondo phenomena²² are observed neither in the normal nor in the superconducting state.

Thermally activated transport– For quantum dots connected to superconducting leads, transport is usually blocked in the energy gap range $|eV_{sd}| \leq 2\Delta$. At high temperature, transport becomes possible both at low bias and in parts of the Coulomb blockade region due to quasiparticles excited across the superconducting energy gap.¹³ This is illustrated in Fig. 1(c), showing the product (black solid line) of the quasiparticle density of states (blue dash-dotted line) and the Fermi function (red dotted line). For sufficiently high temperature, corresponding to a thermal broadening of the Fermi function of the order of the gap, a small peak at $E \approx \Delta$ emerges. This peak vanishes at low temperature when the broadening of the Fermi function is much smaller than the gap. The focus of this work is the systematic investigation of features due to this extra thermal channel, both from the theoretical and experimental point of view. In the following we distinguish between *standard* resonance lines, which are also present at low temperatures, and *thermal* lines due to the presence of the extra thermal peak.

Fig. 2(a)-(c) displays detailed measurements of the differential conductance at increasing temperatures, close to

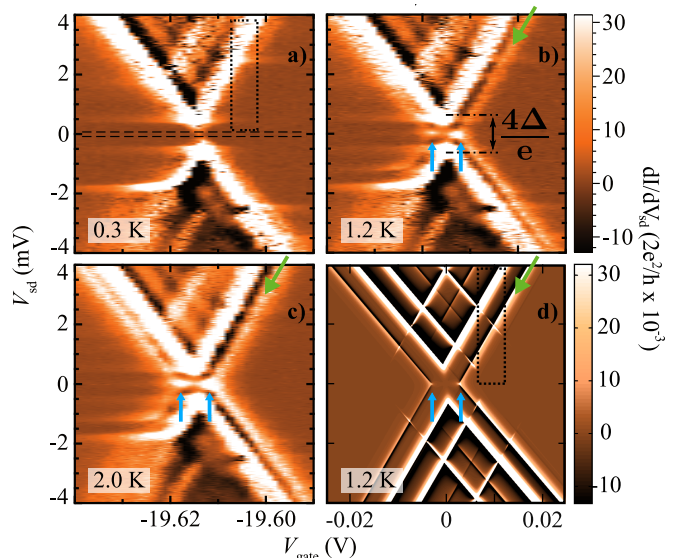


FIG. 2. (Color online) Differential conductance $dI(V_{sd}, V_{gate})/dV_{sd}$ as a function of source-drain voltage V_{sd} and gate voltage V_{gate} measured at (a) $T = 0.3 \text{ K}$, (b) $T = 1.2 \text{ K}$, (c) $T = 2.0 \text{ K}$, and (d) corresponding transport calculation at $T = 1.2 \text{ K}$. One of the additional lines emerging at high temperature is marked by a diagonal green arrow. Around zero bias two conductance peaks are clearly visible (vertical blue arrows). The dotted rectangles in (a) and (d) as well as the horizontal lines in (a) frame regions used to extract the line plots in Figs. 4(a) and (c). The maximum of the dI/dV_{sd} scale was set to $0.031 \times 2e^2/h$ to increase the contrast of the thermally induced lines.

the charge degeneracy point marked by the black rectangle in Fig. 1(b).²³ The comparison of Fig. 2(a) and Figs. 2(b) and (c) gives direct evidence that at temperatures above $T \simeq 300 \text{ mK}$ additional transition lines parallel to the sequential tunneling lines emerge within the region of Coulomb blockade, see e.g. the green arrow in Fig. 2(b)-(d). These lines are separated from the sequential tunneling lines by a characteristic region of negative differential conductance (NDC, dark). As can be seen in Fig. 2(d), the additional lines and the NDC regions are reproduced by our transport calculations described in detail below, which account for sequential tunneling processes of thermally excited quasiparticles. At the intersection of such lines we obtain two zero bias conductance peaks indicated by blue arrows and separated by $\delta V_g = 2|\Delta|/e\alpha_g$, with α_g as the gate coupling factor.

Theoretical model– Our calculations are based on a master equation approach for the reduced density matrix (RDM) to lowest order in the tunneling to the leads, including only quasiparticle tunneling.¹³ The theory is generalized here to include also the shell and orbital degrees of freedom of the CNT. Specifically, the quantum dot is modeled by the Hamiltonian

$$\hat{H}_{\text{CNT}} = \sum_{\alpha\sigma} \epsilon_{\alpha\sigma} \hat{d}_{\alpha\sigma}^\dagger \hat{d}_{\alpha\sigma} + \frac{U}{2} \hat{N} (\hat{N} - 1), \quad (1)$$

where $\alpha = (s, \tau)$ is a collective quantum number accounting for longitudinal (s) and orbital (τ) degrees of freedom, respectively, and σ labels the spin.²⁴ Finally, we employ a constant interaction model for the Coulomb repulsion on the tube with strength U . Including two longitudinal modes, $s = 1, 2$, and accounting for the two orbital degrees of freedom, $\tau \in \{a, b\}$, of the CNTs, $\epsilon_{\alpha\sigma}$ represents four energy levels with energies ϵ_0 , $\epsilon_0 + \delta$, $\epsilon_0 + \Delta\epsilon$, and $\epsilon_0 + \Delta\epsilon + \delta$. The characteristic fourfold degeneracy of the carbon nanotube spectrum is assumed to be lifted by $\delta = \sqrt{\Delta_{\text{SO}}^2 + \Delta_{\text{KK}}^2}$, originating from spin orbit splitting Δ_{SO} and valley-mixing Δ_{KK} .²⁵

The size of the experimentally measured Coulomb diamonds and the positions of the excited state lines in the stability diagrams are consistent with the assumption that the transitions occur between states with $(4n + 3)$ and $(4n + 4)$ electrons. They are correctly reproduced in our model with $\delta = 1.3$ meV, a spacing between the longitudinal modes $\Delta\epsilon = 1.55\delta$, and $U = 15$ meV. The gate voltage is assumed to linearly shift the single particle energy levels $\epsilon_{\alpha\sigma} \rightarrow \epsilon_{\alpha\sigma} + \alpha_g eV_g$. At finite bias voltage the electrochemical potentials in the source and drain electrodes are $\mu_{\text{S/D}} = \mu_0 \pm \alpha_{\text{S/D}} eV_b$, where $\alpha_{\text{S}} = \alpha_{\text{sd}}$ and $\alpha_{\text{D}} = 1 - \alpha_{\text{sd}}$ account for the asymmetric bias drop at the source and drain contact, respectively. From our simulations, we find an effective back gate coupling $\alpha_g = 0.1$ and an asymmetric bias drop $\alpha_{\text{sd}} = 0.4$.

The expected positions of the differential conductance lines of the stability diagrams are displayed in Fig. 3(a). The solid blue lines show the $(4n + 3)$ electron ground state to $(4n + 4)$ electron ground state transition $(3_g)-(4_g)$, the broken blue lines are instead transition lines between a ground state and an excited state of the neighbouring particle number, see Fig. 3(b). Each of the possible standard transition lines is accompanied by an associated thermal line (in orange, same line style) due to thermally activated quasiparticles. We set the zero of the gate voltage at the charge degeneracy point. The position of the blue transition lines is then dictated by the standard sequential tunneling requirements,¹³

$$eV_{\text{sd}} = \frac{1}{\alpha_{\text{S/D}}} \left(\pm \alpha_g eV_g + \Delta E + |\Delta| \right), \quad (2)$$

for source lines (+) and drain (-) lines. Here, ΔE is the energy difference between an excited state and a ground state with the same particle number in the many-body spectrum of Fig. 3(c). In the case of a source (drain) transition ΔE is calculated in the N ($N + 1$) particle subspace. For a ground state to ground state transition, $\Delta E = 0$ in Eq. (2).

The conditions for the occurrence of an orange thermal line are

$$eV_{\text{sd}} = \frac{1}{\alpha_{\text{S/D}}} \left(\pm \alpha_g eV_g + \Delta E - |\Delta| \right). \quad (3)$$

Thus, each replica runs parallel to the diamond edge at a distance $2|\Delta|/\alpha_{\text{S/D}}$ from the standard line associated to it.

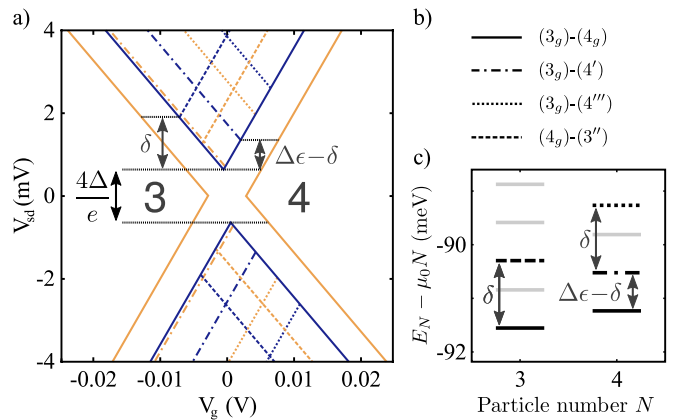


FIG. 3. (Color online) (a) Expected position of the differential conductance lines of the stability diagram in Fig. 2(d). The solid blue (dark gray) lines correspond to standard transitions between the $(4n + 3)$ - and $(4n + 4)$ -electron ground states, denoted (3_g) and (4_g) , respectively. The solid orange (light gray) lines are caused by thermally activated transport channels. Lines from standard transitions involving an excited state are depicted as broken blue lines, the associated thermal replica in orange with the same line style. (b) Legend associating transition lines to transitions between states. We denoted the first, second, and third excited state of electron number N by (N') , (N'') , and (N''') , respectively. (c) Many-body spectrum of the $(2n + 3)$ and $(2n + 4)$ electron subspace as observed in transport, for $\alpha_g eV_g = |\Delta|$. Here the 3-particle groundstate energy is $E_3^g - 3\mu_0 = -2\delta - 6U + 3|\Delta|$. The distances between the energy levels ΔE (cf. Eqs. (2) and (3)), marked by arrows, are used to extract $\Delta\epsilon$ and δ from the measurements. Transitions involving the levels marked light gray are not experimentally observed.

Low bias conductance– Fig. 4(a) shows the gate voltage dependence of the low bias differential conductance for increasing temperature. Each trace is an average of several measurements taken at small but finite bias values symmetrically located around $V_{\text{sd}} = 0$ and corresponding to the area between the dashed horizontal lines in Fig. 2(a). Note that due to the existence of a superconducting energy gap, no current would be expected in this bias voltage range. Two clearly distinguishable peaks are observed. They result from the zero-bias crossing of the thermally induced transition lines. Due to their thermal nature, they decrease for decreasing temperature. At $T = 0.3$ K the double peak is absent. A single peak observed at approximately the position of the charge degeneracy point may be due to higher order processes not captured by the theory discussed below.

In Fig. 4(b) the maximal conductance measured at the two peaks denoted by A and B in Fig. 4(a) is plotted as a function of the temperature (squares and triangles, respectively). The observed behaviour is well reproduced by an analytic expression for the linear conductance derived around the N to $(N + 1)$ charge degeneracy point (solid lines). By taking into account the ground state energy levels of the relevant N and $N + 1$ -particles sub-

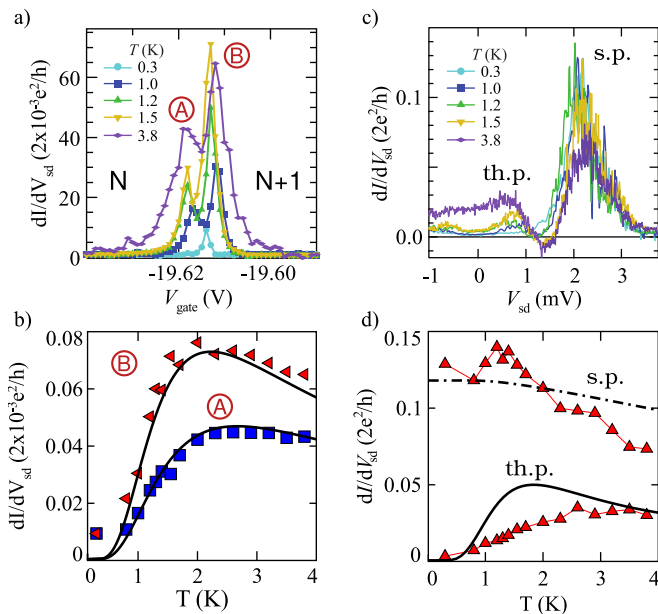


FIG. 4. (Color online) (a) Gate voltage dependence of the low bias conductance at different temperatures. Each trace is an average over the bias voltage region marked in Fig. 2(a). (b) Temperature dependence of the conductance maxima A (squares) and B (triangles) in Fig. 4(a), together with a model calculation according to Eq. (4) (lines). (c) Bias traces of the differential conductance, taken within the rectangular area in Fig. 2(a), for different temperatures (see text). Two peaks due to standard (s.p.) and thermal (th.p.) processes are observed. (d) Temperature dependence of the maximum of the differential conductance peaks of Fig. 4(c). The solid and the dash-dotted line result from corresponding model calculations using a corresponding average. Our second order theory is overestimating the peak height of the standard peak. Hence the curve was multiplied by 0.28 for a better qualitative comparison.

space, we find

$$\left. \frac{dI}{dV_{sd}} \right|_{V_{sd}=0} = \frac{e^2}{2} \frac{\Gamma}{k_B T} \operatorname{Re} \left(\cosh \left(\frac{\Delta E_g + i\gamma}{2k_B T} \right) \right)^{-2} \times D(\Delta E_g) (\rho_N + \rho_{N+1}), \quad (4)$$

with the BCS density of states $D(E)$, and the occupation probability of the N -particle ground state ρ_N . The energy difference ΔE_g between the two ground states scales linearly with V_{gate} and equals zero at the charge degeneracy point. Here, γ is a phenomenological Dynes parameter²⁶ related to a finite lifetime of the quasiparticles in the superconducting leads. The Dynes parameter is introduced to renormalize the BCS density of states and therefore leads to a broadening of the conductance peaks. Eq. (4) predicts the existence of two maxima of the conductance located symmetrically around $\Delta E_g = 0$. The values of the maxima as a function of the temperature correspond to the two solid lines in Fig. 4(b).

We notice a good agreement between experiment and theory at temperatures above $T \sim 1$ K. From the fit we

extract the coupling parameter $\Gamma = 0.093$ meV and the Dynes parameter $\gamma = 0.015$ meV. The temperature dependence of the conductance peaks can be divided into two regimes. At low temperature, i.e., in the thermal activation regime, the “ \cosh^{-2} ” term of Eq. (4) dominates, leading to a steep increase of the peaks with temperature. In the high temperature regime, we see the typical $1/T$ decay known from standard sequential tunneling processes.²⁷

Of particular interest is the ratio of the conductance maxima of the left and the right peak. Since Eq. (4) is symmetric around $\Delta E_g = 0$, we find that the ratio is equal to

$$\frac{dI/dV_{sd}^A}{dI/dV_{sd}^B} = \frac{(\rho_N + \rho_{N+1})_A}{(\rho_N + \rho_{N+1})_B} = \frac{d_{N+1} + d_N e^{-\Delta E_g/k_B T}}{d_N + d_{N+1} e^{-\Delta E_g/k_B T}}, \quad (5)$$

where canonical expressions were used for the occupation probabilities ρ_N and ρ_{N+1} , and d_N (d_{N+1}) denotes the degeneracy of the N and $(N+1)$ particles ground state. Thus, it is possible to directly probe the degeneracy of the two ground states using Eq. (5). Fig. 4(a) and (b) show that the conductance at point (B) is larger than at point (A), leading to the conclusion that the N -particles ground state has a larger degeneracy than the $N+1$ -particles ground state. This confirms the assumption that the data are measured around a $(4n+3)$ - $(4n+4)$ type charge degeneracy point, as also supported by the correspondence between the theory and experiment of excited state transition lines (see Fig. 2).

According to our model, the four fold degeneracy of the CNT is broken and the degeneracy of a ground state with odd number of particles, due to time reversal symmetry, equals $d_{2N+1} = 2$. Taking the ratio of the measured peak height of the two thermally induced conductance peaks provides, to our knowledge, a new method to determine the degeneracy of the ground state of multi-electron quantum dot single electron transistors.

Finite bias conductance– The behavior of thermal and standard transitions at finite bias is depicted in Fig. 4(c), which shows $dI/dV_{sd}(V_{sd})$ traces at various temperatures. These traces result from an average taken over the voltage range marked by the dotted box in Fig. 2(a).²⁸ We observe two peaks which evolve in opposite ways at increasing temperature: the standard peak (s.p.) at higher V_{sd} decreases as expected from standard sequential tunneling.²⁷ The second one at lower V_{sd} increases and hence confirms thermally assisted quasiparticle tunneling (thermal peak, th.p.). A characteristic dip evolving into NDC is also clearly observed in the line traces in Fig. 4(c).

In Fig. 4(d) the extracted temperature dependence of both the thermally activated and the standard sequential tunneling peak is depicted (triangles). Similar to the data analysis of the experiments, also the theoretical curves for the peak height were calculated via averaging over the voltage range marked with the dotted rectangle in Fig. 2(d). Our perturbative theory is overestimating

the height of the standard peak. Hence, the theoretical curve (dash-dotted line) was multiplied by 0.28 to allow a better comparison with experimental data. A decrease of the peak is observed with increasing temperature. The calculation for the thermally activated peak (solid black line) is in good agreement with experiments; it shows a similar temperature dependence as the conductance peaks in Fig. 4(b).

Preliminary calculations show that a renormalization of the lowest order theory taking into account also charge fluctuations in the framework of a dressed second order theory²⁹ can reproduce the broadening (linewidth) of the resonance peaks and gives the correct ratio between the peak height of the thermally induced and the standard sequential tunneling peak. This study will be the subject

of an upcoming publication.

Conclusions— We demonstrate thermally activated quasiparticle transport in a carbon nanotube quantum dot with superconducting contacts. Our theoretical analysis shows that the new lines in the otherwise blocked regions of the stability diagram appear already in the sequential tunneling regime. The splitting of the thermally induced conductance peaks at low bias can be used to probe the degeneracy of the ground states, and provides a particularly useful method to determine charge configurations from transport characteristics.

The authors would like to thank Kicheon Kang for insightful discussions. We acknowledge funding from the Deutsche Forschungsgemeinschaft (SFB 631 TP A11, GRK 1570, Emmy Noether project Hu 1808-1) and from the EU FP7 Project SE2ND.

-
- * sebastian1.pfaller@ur.de
† christoph.strunk@ur.de
- ¹ M. Bockrath, D. H. Cobden, P. L. McEuen, N. G. Chopra, A. Zettl, A. Thess, and R. E. Smalley, *Science* **275**, 1922 (1997).
 - ² A. Jensen, J. R. Hauptmann, J. Nygård, and P. E. Lindelof, *Phys. Rev. B* **72**, 035419 (2005).
 - ³ A. Kasumov, M. Kociak, M. Ferrier, R. Deblock, S. Guéron, B. Reulet, I. Khodos, O. Stéphan, and H. Bouchiat, *Phys. Rev. B* **68**, 214521 (2003).
 - ⁴ K. Grove-Rasmussen, H. I. Jørgensen, B. M. Andersen, J. Paaske, T. S. Jespersen, J. Nygård, K. Flensberg, and P. E. Lindelof, *Phys. Rev. B* **79**, 134518 (2009).
 - ⁵ J.-P. Cleuziou, W. Wernsdorfer, V. Bouchiat, T. Ondarcuhu, and M. Monthieux, *Nat. Nanotech.* **1**, 53 (2006).
 - ⁶ P. Jarillo-Herrero, J. A. van Dam, and L. P. Kouwenhoven, *Nature* **439**, 953 (2006).
 - ⁷ E. Pallecchi, M. Gaass, D. A. Ryndyk, and C. Strunk, *Appl. Phys. Lett.* **93**, 072501 (2008).
 - ⁸ T. Dirks, T. L. Hughes, S. Lal, B. Uchoa, Y.-F. Chen, C. Chialvo, P. M. Goldbart, and N. Mason, *Nat. Phys.* **7**, 386 (2011).
 - ⁹ J.-D. Pillet, C. H. L. Quay, P. Morfin, C. Bena, A. L. Yeyati, and P. Joyez, *Nat. Phys.* **6**, 965 (2010).
 - ¹⁰ B.-K. Kim, Y.-H. Ahn, J.-J. Kim, M.-S. Choi, M.-H. Bae, K. Kang, J. S. Lim, R. López, and N. Kim, *Phys. Rev. Lett.* **110**, 076803 (2013).
 - ¹¹ J.-D. Pillet, P. Joyez, R. Žitko, and M. F. Goffman, *Phys. Rev. B* **88**, 045101 (2013).
 - ¹² A. Kumar, M. Gaim, D. Steininger, A. Levy Yeyati, A. Martín-Rodero, A. K. Hüttel, and C. Strunk, *Phys. Rev. B* **89**, 075428 (2014).
 - ¹³ S. Pfaller, A. Donarini, and M. Grifoni, *Phys. Rev. B* **87**, 155439 (2013).
 - ¹⁴ J. Kong, H. Soh, A. Cassell, C. Quate, and H. Dai, *Nature* **395**, 878 (1998).
 - ¹⁵ J. M. Martinis and R. L. Kautz, *Phys. Rev. Lett.* **63**, 1507 (1989).
 - ¹⁶ S. De Franceschi, S. Sasaki, J. M. Elzerman, W. G. van der Wiel, S. Tarucha, and L. P. Kouwenhoven, *Phys. Rev. Lett.* **86**, 878 (2001).
 - ¹⁷ J. V. Holm, H. I. Jørgensen, K. Grove-Rasmussen, J. Paaske, K. Flensberg, and P. E. Lindelof, *Phys. Rev. B* **77**, 161406 (2008).
 - ¹⁸ An evaluation of the elastic cotunneling lines in Fig. 1(b), not within the scope of our lowest-order theory, results in a slightly reduced value $\Delta \sim 250 \mu\text{eV}$.
 - ¹⁹ J. K. Hulm, C. K. Jones, R. A. Hein, and J. W. Gibson, *Journal of Low Temperature Physics* **7**, 291 (1972).
 - ²⁰ S. De Franceschi, L. Kouwenhoven, C. Schönenberger, and W. Wernsdorfer, *Nat. Nanotech.* **5**, 703 (2010).
 - ²¹ M. Buitelaar, W. Belzig, T. Nussbaumer, B. Babić, C. Bruder, and C. Schönenberger, *Phys. Rev. Lett.* **91**, 057005 (2003).
 - ²² D. Goldhaber-Gordon, J. Göres, M. A. Kastner, H. Shtrikman, D. Mahalu, and U. Meirav, *Phys. Rev. Lett.* **81**, 5225 (1998).
 - ²³ An apparent discrepancy in gate voltage range between Fig. 1(b) and Fig. 2(a)-(c) is due to long-time scale uniform drift of all Coulomb blockade features. The conductance peaks have been re-identified from overview measurements.
 - ²⁴ The term longitudinal mode is referring to the energy quantization associated to the finite length of the carbon nanotube. The Hamiltonian in Eq. (1) includes both spin orbit interaction and KK' mixing terms. Since it is written in the diagonal basis, the quantum number τ is accounting for the “orbital” degrees of freedom, which are linear combinations of states in the KK' basis.²⁵
 - ²⁵ K. Flensberg and C. M. Marcus, *Phys. Rev. B* **81**, 195418 (2010).
 - ²⁶ R. C. Dynes, V. Narayanamurti, and J. P. Garno, *Phys. Rev. Lett.* **41**, 1509 (1978).
 - ²⁷ C. W. J. Beenakker, *Phys. Rev. B* **44**, 1646 (1991).
 - ²⁸ In order to not introduce an artificial broadening in the average, since the conductance peaks lie at different V_{sd} for different values of V_{gate} , the curves were shifted to compensate for that offset. The reference with respect to which all other curves were shifted was always the curve closest to the degeneracy point. Repeating that procedure for different temperatures yields Fig. 4(c).
 - ²⁹ J. Kern and M. Grifoni, *Eur. Phys. J. B* **86**, 384 (2013).